

## Experimental and Numerical Analysis of Triaxially Braided Composites Utilizing a Modified Subcell Modeling Approach

Christopher Cater and Xinran Xiao

*Composite Vehicle Research Center, Michigan State University, Lansing, MI*

Robert K. Goldberg and Lee W. Kohlman

*NASA Glenn Research Center, Cleveland, OH*

### ABSTRACT

A combined experimental and analytical approach was performed for characterizing and modeling triaxially braided composites with a modified subcell modeling strategy. Tensile coupon tests were conducted on a  $[0^\circ/60^\circ/-60^\circ]$  braided composite at angles of  $0^\circ$ ,  $30^\circ$ ,  $45^\circ$ ,  $60^\circ$  and  $90^\circ$  relative to the axial tow of the braid. It was found that measured coupon strength varied significantly with the angle of the applied load and each coupon direction exhibited unique final failures. The subcell modeling approach implemented into the finite element software LS-DYNA was used to simulate the various tensile coupon test angles. The modeling approach was successful in predicting both the coupon strength and reported failure mode for the  $0^\circ$ ,  $30^\circ$  and  $60^\circ$  loading directions. The model over-predicted the strength in the  $90^\circ$  direction; however, the experimental results show a strong influence of free edge effects on damage initiation and failure. In the absence of these local free edge effects, the subcell modeling approach showed promise as a viable and computationally efficient analysis tool for triaxially braided composite structures. Future work will focus on validation of the approach for predicting the impact response of the braided composite against flat panel impact tests.

### INTRODUCTION

Two dimensional (2D) triaxially braided composites are increasingly used in a wide variety of high-performance applications which require both the improved specific stiffness and strength of carbon fiber composites and the delamination resistance and impact toughness of a textile reinforcement architecture [1]. This composite reinforcement is widely used in aircraft structural components such as the fan containment system of turbine engines for which the dynamic and impact properties of the composite are crucial [2].

To consider the meso-scale heterogeneity in FEA, a subcell approach has been proposed [3-8]. The subcell approach has several added benefits over traditional composite modeling methods. Firstly, the preservation of macroscale heterogeneity sets it apart from standard multiscale schemes, which typically define the macroscale as an orthotropic, homogeneous medium. For triaxially braided composites, the braided pattern is too large to not be accounted for in the finite element analysis at the macroscopic scale. The subcell approach provides continued heterogeneity at the highest scale. Secondly, the semi-analytical nature of the subcell discretization allows for improved computational efficiency over complex representative unit cell (RUC)

models of textile reinforced composites or the explicit meso-scale modeling of braided coupons. Both of these advantages are central to any modeling approach aiming to efficiently capture impact damage patterns shown to be dependent on the braided architecture of multi-layer triaxial braids [2].

Although the subcell approach has been investigated by several researchers, it is still in the development stage and a comprehensive evaluation is ongoing. In this work, a combined experimental and numerical approach is undertaken to verify the efficacy of the subcell modeling approach in capturing the characteristics of a 2D triaxially braided composite. A suite of straight sided coupon tests per ASTM standards was conducted for a variety of coupon angles, including  $0^\circ$ ,  $30^\circ$ ,  $45^\circ$ ,  $60^\circ$  and  $90^\circ$ . Previous work present in the current literature has only investigated the axial ( $0^\circ$ ) and transverse ( $90^\circ$ ) directions of the braided composite [9]. These results will be used to evaluate the efficacy of the computationally efficient subcell modeling approach in capturing the experimental coupon strengths and failure modes as a function of the change in coupon orientation. First, the subcell model development is outlined. Second, the characterization processes for determining material parameters of the material model within the dynamic finite element package LS-DYNA are discussed. Next, the experimental results are presented for the off-axis coupon tests. Finally, the simulation results are presented, along with modified improvements and a discussion of the presented results.

## **SUBCELL MODEL**

### **Subcell Discretization**

The subcell approach is outlined in Fig. 1. First, the RUC is identified and partitioned into subcell regions. The four subcells shown in Fig.1 correspond to the regions where axial ( $0^\circ$ ) and braider ( $+60^\circ/-60^\circ$ ) tows were both present (subcells A and C) and regions where only braider tows were present (subcells B and D) [3-6,7,8]. In this discretization, subcells A and C had identical fiber content and differed only in the arrangements of the braider tows. The same relation is true for subcells B and D. After the establishment of subcells, the next step is to discretize the subcells using a “mosaic” approach. Thus, each subcell is approximated as a unique composite laminate which can be modeled as a laminated composite shell. By modeling each subcell as a laminated composite shell, the meso-scale heterogeneity can be preserved in the macro-scale FE model.

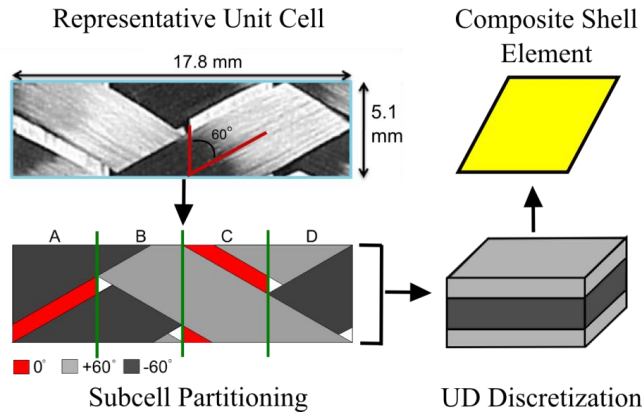


Figure 1. Workflow of the semi-analytical subcell approach. The representative unit cell of the braided composite is partitioned into various subcells which are then discretized into a unidirectional (UD) ply approximation. The resulting subcell is modeled as a composite shell element in a finite element analysis.

A subcell may be discretized in a number of ways. Figure 2 presents the absorbed matrix model (AMM) which was found to best capture the in-plane and out-of-plane stiffness properties of the braided composite [7]. In Fig. 2, subcells A and C are modeled as unsymmetric laminates while subcells B and D are assumed to be symmetric. The asymmetry allows for the capturing of important tension-twist coupling of the local braided regions during tensile deformations. Additionally in the AMM, it is assumed that the axial ( $0^\circ$ ) plies account for only the fiber tows, whereas the braider ( $\pm 60^\circ$ ) plies are a homogenized representation of the braider tows and surrounding pure matrix regions. This discretization was found to best capture the local fiber volume fraction in each of the subcell regions and differs from other subcell models which modeled pure matrix regions explicitly [6,7].

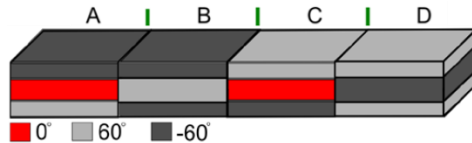


Figure 2. The subcell UD discretization method for the absorbed matrix model (AMM) highlighting the orientation of fibers in the individual lamina layers.

### Determination of Unidirectional Ply Volume Fractions

The calculation of subcell laminate parameters for AMM followed the approach by Cater et al [7]. The first step was to compute the volume of fibers in each subcell. The second step involved determining the volume fractions and respective fiber volume fractions of the unidirectional plies comprising each subcell.

The geometrical parameters of a braided composite system consisting of T700 Toray fibers with Cytec PR 520 resin, hereby referred to as PR520, are provided in Table 1. These values were used to approximate the volume of fibers in each subcell. The subcell widths  $W_A$  and  $W_B$  are measured as shown in Fig. 3a, along with the

subcell length,  $L$ . Figure 3 also shows the amount of braider tow (dashed yellow regions) contained within a given subcell (solid green square). It was assumed, as in Xiao [6], that the lengths  $l_{bB}$  and  $l_{bA}$  can be used in a straight line approximation to account for all of the braider tow contained within the subcell. Figure 3b presents a three-dimensional view highlighting the determination of these braider tow lengths.

TABLE I. GEOMETRICAL PARAMETERS USED FOR CALCULATING THE LAMINA THICKNESSES (T700/PR520 SYSTEM)

Label	Description	Value
$W$	Width of RUC (mm) <sup>a</sup>	8.9
$W_A$	Width of cell A (mm) <sup>a</sup>	4.201
$W_B$	Width of cell B (mm) <sup>a</sup>	4.765
$h$	Ply thickness (mm) <sup>a</sup>	0.56
$V_{f,tow}$	Tow fiber volume fraction <sup>a</sup>	0.8
$n_a$	Number of fibers in axial tow ( $10^3$ ) <sup>b</sup>	24
$n_b$	Number of fibers in braider tow ( $10^3$ ) <sup>b</sup>	12
$d_a$	Diameter of fiber filament in axial tow ( $\mu\text{m}$ ) <sup>b</sup>	7
$d_b$	Diameter of fiber filament in the braider tow ( $\mu\text{m}$ ) <sup>b</sup>	7
$L$	Length of unit cell (mm) <sup>b</sup>	5.1
$\theta$	Braid angle (degrees)	+/- 60

<sup>a</sup> Data obtained from Blinzler [8]

<sup>b</sup> Obtained from product data sheets (<http://www.toraycfa.com/pdfs/T700SDataSheet.pdf>)

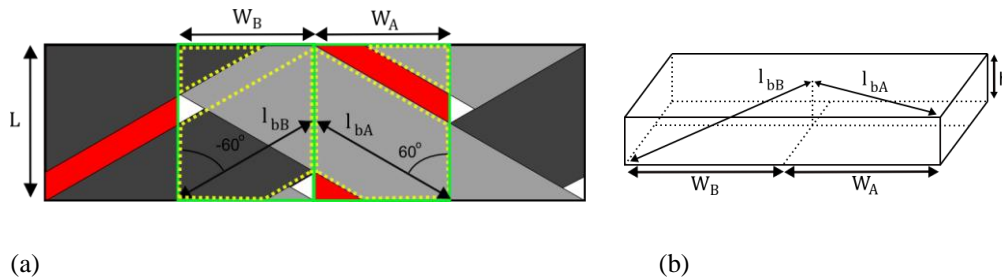


Figure 3. (a) Two unit cells of the braided composite are shown with the widths of subcells A and B labeled. The green boxes represent the size of a subcell. The dotted yellow boxes represent the amount of a single braider tow contained within each subcell volume (each subcell contains two braider tows), determined by the lengths  $l_{bB}$  and  $l_{bA}$ . (b) Schematic of the braider fiber tow lengths approximated by the straight line mode for subcells A and B.

The volume of axial fibers and braider fibers in subcells A and B are computed following the method in [6]. The resulting laminate configurations are presented in Table 2, where the volume fraction of each ply layer is listed as a percentage of the laminate thickness. As a result of the absorbed matrix model, there are three unique unidirectional plies as indicated by the varying fiber volume fractions listed in Table 2 for the T700/PR520 system.

TABLE II. SUBCELL A &amp; B DISCRETIZATION FOR THE ABSORBED MATRIX MODEL

Subcell A Lay-up	Angle (°)	Vf	Thickness (%) <sup>a</sup>
Braider ply	-60	73.3%	25.5
Axial ply	0	80.0%	49
Braider ply	60	73.3%	25.5
Subcell B Lay-up			
Braider ply	-60	37.5%	25
Braider ply	60	37.5%	50
Braider ply	-60	37.5%	25

<sup>a</sup> Percent of overall ply thickness

## Ply Constitutive Model

The effective unidirectional plies were modeled using the continuum damage mechanics material model MAT 58 within the transient dynamic commercial finite element code LS-DYNA. Based on the Matzenmiller-Lubliner-Taylor theory [10], MAT 58 employs an exponential damage law to capture non-linear response of the composite through elastic softening [11].

The effective UD plies were assumed to be linear elastic in longitudinal tension and compression, whereas the transverse and shear directions are assumed to be non-linear. The material model specifies the material strengths and failure strains in the longitudinal (fiber), transverse (matrix) and shear directions, requiring a total of 10 parameters to properly characterize the material response in tension, compression and shear (5 stresses and 5 corresponding strain values).

In MAT 58, either a faceted failure surfaces based on Hashin criterion or a smooth, Tsia-Wu type of failure surface are available. The Hashin criterion was selected to uncouple damage in the transverse and shear directions since the plies do not necessarily represent true lamina, and the actual coupling between normal and shear directions is unknown a-priori.

## Effective Unidirectional Ply Stiffness

Since the UD layers and their relative fiber volume fractions are based on the prescribed subcell discretization and not on actual lamina, there are no experimental means by which one can determine their elastic properties. Thus, the mechanical properties of each UD lamina must be computed using a bottom-up micromechanics approach. The micro-constituent properties (fiber and matrix) and their relative volume fractions were then utilized to calculate the moduli and Poisson's ratio of the effective UD layers in each of the subcells.

The micromechanics software MAC/GMC 4.0 developed at NASA Glenn Research Center [12] based on the Generalized Method of Cells [13] was used to compute the effective properties of the UD laminate for this study. The bottom-up, micromechanics approach had been proven to be sufficient to characterize the elastic properties of the braided composite [6,7] since the UD discretization of the subcell approach accurately captures the contribution of fibers in the macro-scale material coordinate system (particularly for in-plane loading).

The process of determining the UD lamina properties was then repeated depending on the number of UD volume fractions present in the discretization. The constituent properties listed in Table 3 along with the fiber volume fractions for the three ply regions, identified in Fig. 4, were used as input for the MAC/GMC homogenization process. The resulting elastic unidirectional properties are presented in Table 4 for the T700/PR520 system.

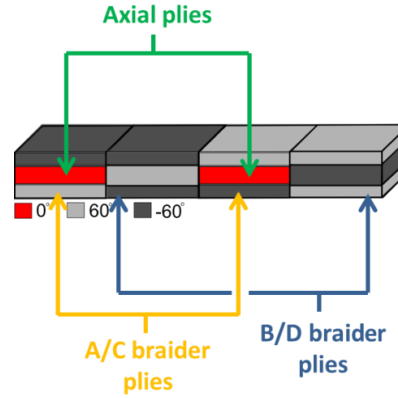


Figure 4. The absorbed matrix subcell model with the three unique UD ply regions highlighted. The labeled regions (Axial, A/C braider and B/D braider) are UD plies with varying fiber volume fractions.

TABLE III. CONSTITUENT MATERIAL PROPERTIES [8,9]

Material	Density, $\text{g}\cdot\text{cm}^{-3}$	$E_{11}$ , GPa	$E_{22}$ , GPa	$\nu_{12}$	$G_{12}$ , GPa
T700 (Fiber)	1.8	230	15	0.2	27
PR520 (Matrix)	1.25	4.0	4.0	0.38	1.44

TABLE IV. EFFECTIVE PLY PROPERTIES FOR THE THREE UNIQUE PLY REGIONS

Description	UD $V_f$	$E_{11}$ , GPa	$E_{22}$ , GPa	$E_{33}$ , GPa	$G_{23}$ , GPa	$G_{13}$ , GPa	$G_{12}$ , GPa	$\nu_{12}$
B-Braider	37.50%	88.5	6.22	6.22	2.04	2.86	2.6	0.3
A-Braider	73.30%	169.5	9.9	9.9	3.4	8.68	7.0	0.23
A-Axial	80%	184.7	10.9	10.9	3.39	10.88	6.0	0.24

### Effective Ply Strengths

For a UD ply, the material strengths are the longitudinal (fiber) tension, longitudinal compression, transverse (matrix) tension, transverse (matrix) compression, and shear. In this study, the two longitudinal strengths were determined using a top-down approach whereas the remaining three strengths were determined using a bottom-up approach.

### Top-Down Unit-Cell Approach

In order to establish the top-down characterization of UD ply strengths, two key assumptions needed to be addressed.

The first assumption was that experimental strength values are intrinsic material properties unique to the braid architecture and to a specific global loading. By taking macroscopic experimental strengths (i.e. axial tensile strength, axial compressive strength, etc.) as an intrinsic material property, one could now resolve the strength determination problem to a Unit-Cell (UC) problem. The UC for the subcell model consisted of an RUC containing all four subcells, and periodic boundary conditions (PBCs) applied along the boundary to simulate the response of the braided composite. The application of PBCs on the Unit-Cell neglected edge effects associated with finite coupon dimensions, although these effects were present in the actual experiments.

The second assumption was that the main macro- or meso-scopic failure mechanisms observed in the experimental tests could be linked, or approximated to, failure of a particular ply. Consequently, the ply strengths could be found by loading the UC to the prescribed macroscopic stress state and determining the level of stress in the “failed” ply. For example, the axial tensile failure of the T700/PR520 braided coupon was dominated by axial tow failure, and the longitudinal strength of the axial plies were calibrated accordingly. Care had to be taken to avoid using experimental coupon tests whose failure was influenced by free edge effects - e.g. transverse, straight-sided tensile tests [9] and shear tests [14] in the triaxial braid – and tests that exhibit multiple, mixed modes of failure.

A schematic of the top-down approach is presented in Fig. 5.

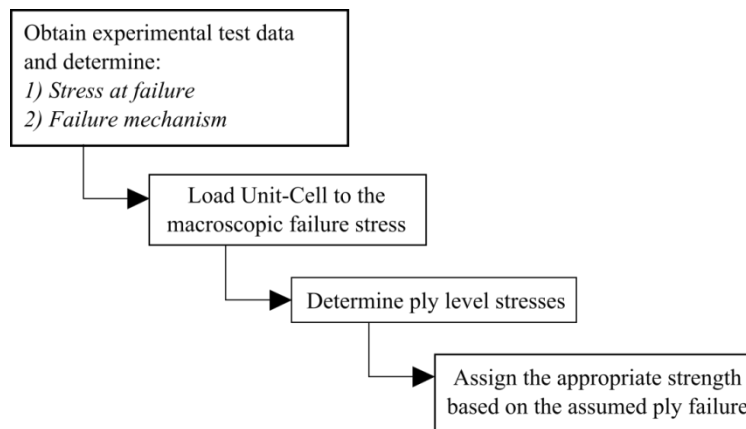


Figure 5. Workflow of the top-down approach for determining ply level strengths.

The proposed workflow assumes that there are no identifiable failures in the experimental test prior to final failure. Material systems and experimental tests which exhibit macroscopic non-linearity as a function of damage would require additional considerations to the proposed workflow.

The UC used for the strength determination process is shown in Fig. 6. The application of periodic boundary conditions followed the form presented by van der Sluis et al. [15] and is represented by Eq. 1. These nodal constraints were defined in the finite element software through the use of linear constraint equations. The displacements of the vertex nodes are given as  $v_{xi}$ , where  $x$  specifies the node and

$i=1,2,3$  are the displacement degrees of freedom. The only independent vertices are  $v_2$  and  $v_3$ . The variable  $\Gamma_{xi}$  corresponds to the displacements along the labeled surface. The first two equations in Eq.1 refer to constraints prescribed between periodic pairs of nodes on opposing surfaces.

$$\begin{aligned} \Gamma_{2i} - \Gamma_{3i} &= v_{2i}, \text{ for } i = x, y, z \\ \Gamma_{4i} - \Gamma_{1i} &= v_{3i}, \text{ for } i = x, y, z \\ v_{4i} &= v_{3i} + v_{2i}, \text{ for } i = x, y, z \\ v_{1i} &= 0, \text{ for } i = x, y, z \end{aligned} \tag{1}$$

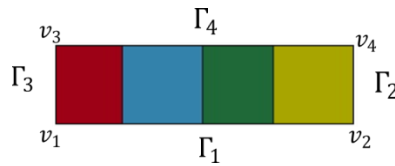


Figure 6. Unit-Cell (UC) used for the determination of ply strengths. The vertices and surfaces used for employing periodic boundary conditions are identified in the figure.

Based on the coupon level strength results [14], four experiments were selected to determine the necessary ply strengths in the longitudinal (fiber) direction. These were the axial tensile and compressive tests, notched transverse tensile test, and transverse compressive test. Figure 7 summarizes the identified failure mechanisms in the experimental tests, the prescribed UC loading and the assigned ply failure.

Experimental Test	Failure Mechanism	Unit-Cell Loading	Assigned Ply Failure
Axial Tension (T) and Axial Compression (C)	Axial Tow Failure		Longitudinal Axial Ply Failure (T/C)
Notched Transverse Tension	Braider Tow Failure		Longitudinal Braider Ply Failure (T)
Transverse Compression	Braider Tow Failure		Longitudinal Braider Ply Failure (C)

Figure 7. Summary of experimental coupon tests used to determine the longitudinal ply strengths.

A limitation of this top-down approach was that failure modes have to be singular and the material response linear-elastic for a given coupon test. Consequently, only coupon tests dominated by longitudinal tow failures could use to determine ply strengths. The straight sided transverse tensile tests of the braided coupon, for example, could not be utilized; the failure was complex, shear dominated and the coupon response was non-linear. Two methods were employed to determine the longitudinal ply strength in tension and both are mentioned here in detail.

In the first approach, strength data taken from notched transverse tensile tests [14] were used to determine longitudinal ply failure of the braider plies in tension as shown



in Fig.7. Using high speed imagery, bias tow failures at the gage section of the transverse notched specimen were found to occur during global failure. The notched transverse tensile test, however, created a bi-axial strain state in the braided composite sections, as observed by Kohlman [14]. To utilize the notched transverse tensile data, the reported strains along the gage section of the composite were averaged in order to determine an approximate biaxial tensile load to apply to the unit cell, as shown in the second row of Fig.7.

Due to short comings in the characterization process from the notched transverse tests – presented and discussed later in this paper, a second approach to obtaining the braider ply strengths in the longitudinal direction was developed. In this approach, the bias ply longitudinal failure strains are set equal to the failure strain of the axial plies in the same material direction (1.9%). Thus, the bias tow tensile failure strain is assumed identical to the axial tow failure strain. This assumption is supported by the fact the longitudinal failure of the tows is fiber dominated. It should be noted that the bias UD plies in subcells A and B differed in fiber volume fraction and modulus, thus these strengths were not identical, although the failure strains were set equal.

Bias ply failures for both longitudinal tension and compression were assumed to be independent of their location (e.g. in subcell A or B), therefore the longitudinal bias ply strengths were assigned simultaneously to the braider plies in all subcells. The axial and transverse compressive strengths for the braided composite were obtained from Kohlman [14] using the standard straight sided coupon tests.

#### *Bottom-up Transverse and Shear Strength*

With the aim of initially populating these unknown UD strengths, the following methods/assumptions were utilized to obtain the three remaining strength parameters. First, bottom-up micromechanics was utilized to characterize the non-linear response of the axial and braider plies in the transverse tensile and shear directions, the two directions dominated by the matrix response. These micromechanics predictions provided the input for the LS-DYNA material model. In these simulations, the fibers were considered linear elastic. For the matrix constitutive response, a nonlinear, strain rate dependent plasticity model which includes the effects of hydrostatic stress was utilized [16].

The full set of material strength and corresponding strain values for the T700/PR520 composite are given in Table 5. The MAC/GMC results for the transverse compressive response for all three ply fiber volume fractions did not produce a specific yield point, or non-linear stress-strain curve to prescribe an appropriate plateau stress, even up to large applied strains of 25-30%. To overcome this limitation in the prescribed matrix constitutive model, a transverse compressive plateau stress was set equal to the shear strength, and a corresponding strain chosen, based on the transverse ply modulus. This is reflected in Table 5 as the strength values of TC. This assumed compressive strength was assigned to ensure that plies did not hold unrealistically high loads in the transverse compressive directions. It should be noted that this transverse compressive failure of the braider tows was not observed in any of the experiments and may not be a critical parameter.

TABLE V. UNIDIRECTIONAL PLY PROPERTIES FOR THE T700/PR520 TRIAXIALLY BRAIDED COMPOSITE IN THE ABSORBED MATRIX MODEL SUBCELL APPROACH

	UD Ply Strength (MPa)						UD Failure Strain		
	LT	LC	TT	TC	SC	TAU1	GAMMA1	ETT2	GMS
Axial Plies	3599	1379	151	195.8	195.8	50.0	0.075	0.032	0.1475
A/C Braider Plies	1648	696	135.0	221	221	201	0.084	0.032	0.16
B/D Braider Plies	938	403	87.7	193.4	193.4	75.0	0.045	0.030	0.300

Note: LT = Longitudinal tension, LC = Longitudinal compression, TT = Transverse tension, TC = Transverse compression, SC = Shear Plateau, TAU1 = First Shear Stress, GAMMA1= First Shear Strain, GMS = Plateau Shear Strain

## EXPERIMENTAL RESULTS

Off-axis tension testing on composite specimens was conducted at the NASA Glenn Research Center in Cleveland, Ohio. The purpose of the testing was to provide additional material characterization of the braided composite as well as validation test cases for the subcell modeling approach. Testing was completed with off-axis orientations of 0°, 30°, 45°, 60°, and 90°. The 0° and 90° tests represent the standard axial and transverse coupon tests used to characterize orthotropic materials. The 30° and 60° directions were chosen since they are aligned perpendicular and parallel, respectively, to the bias fiber tows. The 45° test, similar to the 90°, is not aligned with a fiber tow. The results presented here are for the T700/PR520 composite system.

Subsets of the test specimens were monitored with digital image correlation (DIC) using GOM's ARAMIS system. The coupon axial strain value was determined using a 25.4 mm "virtual" axial strain gage provided within the ARAMIS software. This axial gage was centered on the specimen and was used to compute the elastic modulus and construct the stress-strain curves of the specimens.

The experimental results are organized to compare and contrast all 5 experimental coupon directions. The measured moduli and strengths for the various off axis coupons are provided in Fig.8. As expected, both the 0° and 60° coupons exhibited the highest stiffness, since both coupons have tow continuity between the mechanical grips. The remaining coupons, which do not have tow continuity, had similar moduli values with respect to each other. Aside from the 13% variation between the highest and lowest moduli values, the material remained relatively quasi-isotropic in plane as expected due to the 0°/±60° braiding pattern. The stress-strain response of the 0° and 60° coupons were linear elastic until failure. The remaining three off-axis coupons, conversely, exhibited non-linearity prior to failure. The stress-strain curves for each test angle are shown in Fig. 9.

The strengths, on the other hand, differed significantly across the off-axis angles. The 0° coupon had the highest reported strength at 983 MPa. The 60° coupon exhibited a 12% reduction. The 45° and 90° coupon had strength values merely a half of the axial strength of the braided coupon at 556 MPa and 559 MPa, respectively. The 30° coupon was the worst performing in terms of ultimate strength, with a value of 487 MPa. The scatter in the measured strength values can be attributed to the variation of failure modes associated with each orientation. In addition, the low strength values of the 30°, 45° and 90° coupons were accompanied with non-linear stress-strain behavior as seen in Fig.9.

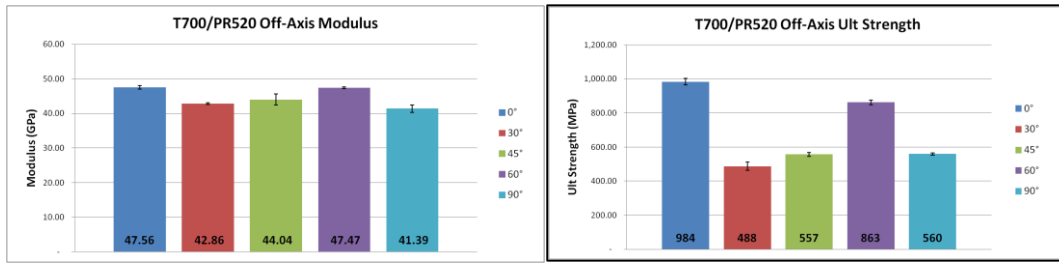


Figure 8. Measured elastic moduli and strengths from the off-axis coupon tests of T700/PR520.






Figure 9. Representative stress-strain curves for the off axis tensile coupon tests of T700/PR520.

The failure morphologies of the tested coupons are summarized in Fig. 10. The 0° and 60° coupons, which exhibited the highest strengths, had the most catastrophic failure and exhibited a minimal residual stiffness/strength after reaching the peak load. Furthermore, the 0° and 60° coupons often had additional compressive failures observed near the grips, which may be a result of the rebounding, post-failure stress wave from the coupon gage section. In both cases, the final failure mechanism was identified as tensile failure of the tow lying parallel to the loading direction. In the 0° coupon, this was the axial tow, whereas for the 60° coupon it was the corresponding bias tow. The failure path in the 0° coupon was transverse to the loading direction, perpendicular to the axial tows as shown in Fig. 10(a). The red dashed line in the figure represents the failure path. The 60° coupon failed in a path preferential along the axial tows (at a 60° angle), as shown in Fig. 10 (d).

The 30° coupon was unique such that it exhibited the highest post-failure residual stiffness (qualitatively) as compared to other coupons. As seen in Fig. 10 (b), the only observed tow failure was of the bias tows lying perpendicular to the loading direction. The fractured surface is rather clean, as indicated by the arrow in the enlarged insert. On the other hand, the tows that did not fracture underwent shifting and pull-out, as seen in the axial tows and other bias tows. The failed, perpendicular bias tows were under compression due to the overall Poisson contraction of the coupon with the macroscopic loading. The clean fracture surface (unlike the frayed fiber tow ends in the tensile failures) is also indicative of compressive failure of these bias tows. The path of bias tow compressive failures were aligned with the axial tow, as seen by the dashed line in Fig. 10 (b), at the point of undulation for the failed bias tow.

Unlike the previous three test cases, the 45° coupon did not exhibit a failure clearly associated with the tensile or compressive failure of a specific tow direction. In Fig. 10 (c), the bias tows near the failed gage section show diffuse splitting and pull-out from the edges of the coupon and several axial tow segments (hidden by the braider tows) had clearly fractured. Since these axial tows oriented 45° degree to the tensile direction, it is hypothesized that the failure of the axial tow is associated with a shear dominated, or a combined, failure in conjunction with bias tow failures initiated from the free edge. Unlike the other cases, a definite failure path could not be determined for the 45° coupons.

The 90° coupon displayed failure morphologies consistent with those described in [14]. The damage was initiated at the free edge, which caused a shear failure. The damage initially was along the axial tow path; however, it jumped to an adjacent axial tow path. An image of the failure is presented in Fig. 10 (e). This phenomenon is likely due to the occurrence of initial cracking at two different locations on the opposing free edges, documented as edge-initiated damage [14]. The two regions met through the shear failure of an axial tow and led to the final failure, as shown by the dashed red-line in Fig. 10 (e).

<p><b>(a) 0° Tensile Test</b></p> <p><b>Failure Notes:</b>          Longitudinal failure of the axial tows.          Catastrophic failure with minimal remaining coupon strength. Failure path looks to be concentrated perpendicular to the loading and axial direction.</p>	
<p><b>(b) 30° Tensile Test</b></p> <p><b>Failure Notes:</b>          Compressive failure of the bias tows lying perpendicular to the applied loading. The failure path of the compressive bias tow failures are along the axial tows and at the point of undulation. The other bias and axial tows remain continuous.</p>	
<p><b>(c) 45° Tensile Test</b></p> <p><b>Failure Notes:</b>          No obvious failure of a specific axial or braider tow. Failure pattern is similar to that of the 90° coupon in that edge damage and shearing look to be a present phenomenon. Shear failure of the axial tow fibers were observed.</p>	

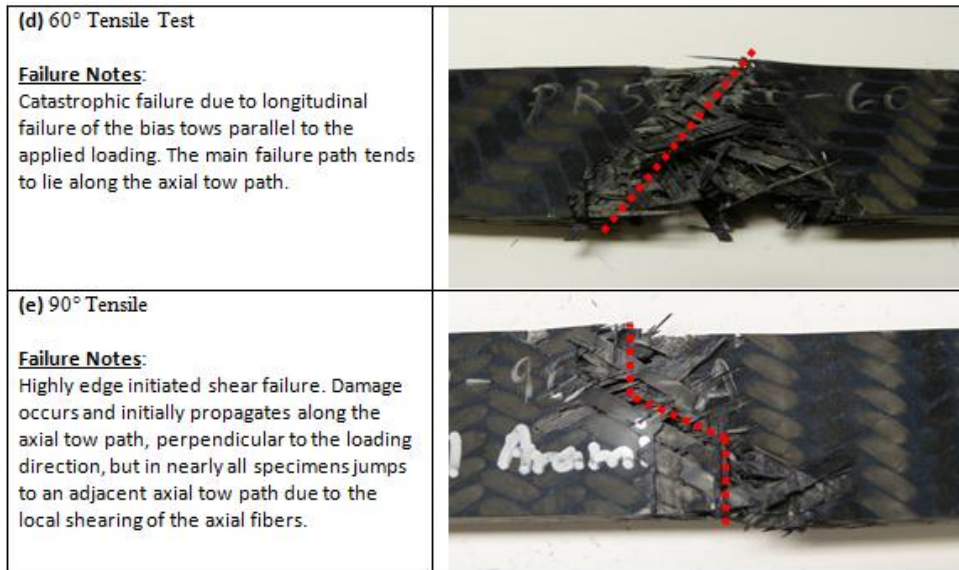


Figure 10. Images of the failed braided coupons along with general notes on failure mechanism.

## FINITE ELEMENT MODEL

The finite element mesh follows the subcell modeling approach, whereby each individual subcell is assigned to a unique composite shell element which contains the appropriate UD stacking and orientations. In LS-DYNA, this is accomplished through the use of the `*Section_Shell` keyword to specify the number of layers and orientations, and the `*Integration_Shell` keyword to specify the material and thickness of each integration point, which in the subcell modeling approach is tied to a given UD layer. Belytskcho-Tsay conventional shell elements were used. The FE mesh is shown in Fig.11, where the 0° and 90° meshes are similar to previous subcell works [5]. For the 30° and 60° coupons, the subcell mesh is skewed, to accomplish the following goals:

- 1) Preserve quadrilateral elements along the free-edge boundaries of the coupons
- 2) Preserve the orientation of the axial tows which are dictated by the red and green element paths shown in the FE mesh.

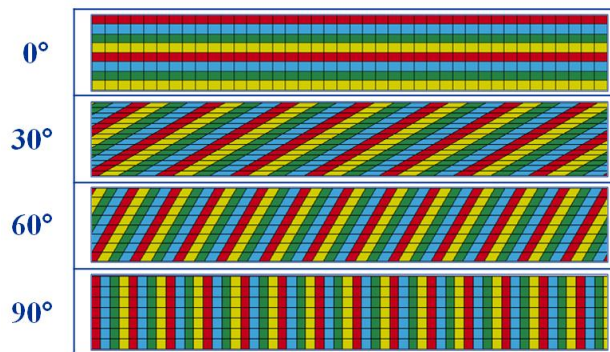


Figure 11. FE mesh of the various off-axis coupons simulated in LS-DYNA. The color coding represents the unique subcell regions (A=Red, B=Blue, C=Green, D=Yellow).

The result of the 45° coupon will be discussed separately in another paper focused on the validation of the subcell approach.

Since free-edge failure was a common, observable phenomenon in the 45° and 90° coupons, measures were taken to ensure that stress-strain calculations at the free-edges would not be distorted by triangular or poorly formed elements. For 30° and 60° coupons, triangular and poorly formed elements do exist at the grip boundaries (not shown). Failure in these regions would invalidate simulation results. Consequently, artificially high strength values are imposed on all elements which are triangular at the gripped boundary or are poorly conditioned. As a result, these regions would behave orthotropic elastic through the entirety of the simulation and force failure to occur away from the gripped boundary. This meshing approach at the gripped boundaries does not conflict with experimental results, since the 30° and 60° coupons failed predominantly at the gage section of the coupon.

The second assumption was made in order to preserve the orientation of the subcell modeling approach, which was preferentially aligned with the axial tow direction. To account for the skewed nature of the subcells, the subcell area was preserved to ensure that the characteristic length associated with the subcells would be consistent across all of the simulations (0° through 90°), thereby eliminating any influence of element size when comparing the simulation results. In general practice, this method of skewing the subcell orientation need only be performed when it is necessary to create a “clean” boundary which does not lie parallel or perpendicular to the axial tow path.

Previous works [7] found that using a single shell element to represent a multi-layer braided coupon did not accurately predict the transverse (90°) modulus of the coupon nor capture the effects of the locally unsymmetric areas. Thus, the six layers of the braided composite were modeled by individual shell layers in this current work. Two different stacking orientations were investigated (perfectly stacked and ideally shifted) as was done in previous subcell studies. The first configuration assumed that axial tows were aligned perfectly through the thickness, whereas the shifted model assumed that an every-other nesting was occurring between the axial tows. A schematic of the ideally shifted model is shown in Fig.12, showing the alternating subcells through the thickness of the coupon. It was found formerly that the two stacking configurations affected the predicted transverse modulus slightly; however, there were no obvious results to conclude preferring one stacking arrangement over the other.

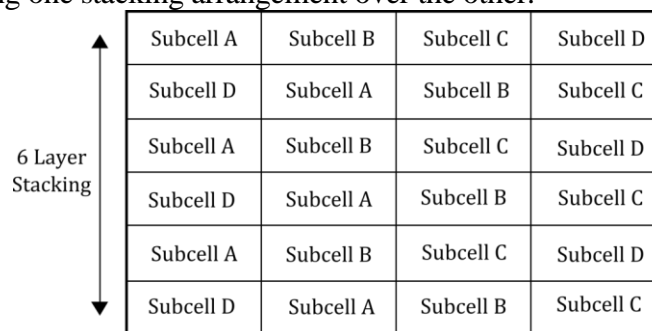


Figure 12. Schematic of the through-thickness ideally shifted coupon stacking. Each row represents a braid layer. The ideally shifted stacking configuration features shifting of the axial subcells (A and C) through the thickness.

In addition to the nesting configuration, the appropriate contact definition between the various plies was investigated. In previous works, a tiebreak contact was employed between shell layers. Nodal constraints would be applied with respect to the translational degrees of freedom only, but would allow for the failure/separation of the nodal constraints upon reaching a failure criterion. This contact definition is hereby referred to as “tiebreak”. The second formulation was a shell-edge to surface constraint which can be applied between node sets along a shell edge and a surface segment. This constraint ties the rotational degrees of freedom and translational degrees of freedom between the shell element nodes and the displacements and curvatures of the respective surface. When applied between the conventional shell layers along with an option to consider distance offsets, it constrains both the rotational and translational degrees of freedom of the two layers. This second contact definition, however, does not allow for failure or separation between layers, and is hereon referred to as the beam offset contact type.

The two contact types will be investigated, along with the two stacking configurations, to understand the influence of each on the coupon behavior and determine the appropriate considerations to take for future impact analysis. No failure is prescribed in the tiebreak contact. The material and model parameters for the T700/PR520 composite are taken as presented from the previous sections on Subcell Modeling.

## **SIMULATION RESULTS & DISCUSSIONS**

The results from the numerical FE model are presented in this section. All strain results were obtained from the LS-DYNA simulations via the use of a virtual strain gage based on the nodal displacements of two nodes located at the mid-section of the coupon. The distance between the two nodes was two unit cells in length (approx 35.6 cm). The stresses were determined via reactionary forces at the applied boundary condition (in the load direction).

### **Shell Contact and Subcell Stacking Configuration Study**

The first set of numerical simulations consisted of both of the two contact definitions between the individual shell layers and the two stacking configurations discussed in the previous section. The results from the 0°, 30°, 60° and 90° coupons are discussed in what follows, however, for brevity not all stress-strain curves are shown.

The predicted strength of the axial (0°) coupons were found to be sensitive to the stacking configuration, with estimations of 892 MPa and 904 MPa for the ideally shifted and perfectly stacked configurations with tiebreak contact, respectively. These values are both slightly lower than the experimentally reported value of 954 MPa. Both the experimental and numerical stress-strain curves were linear elastic until failure, with the simulations showing some non-linearity immediately before failure. This non-linearity, however, was simply a function of the exponential form of damage evolution in the continuum damage mechanics model (MAT 58 in LS-DYNA). The results for the 0° coupon also showed minimal sensitivity with respect to the contact definitions. The tiebreak and beam offset coupons displayed minute differences in moduli and strength for the same stacking configuration.

The results from the 30° coupon are shown in Fig. 13 for all four coupon types alongside the experimental data. The estimated strength of the coupon was found to be insensitive to the stacking configuration as shown below. For example, both the ideally shifted and perfect stack coupons with the beam offset contact definitions exhibited similar ultimate strengths and ductile post-peak responses. The choice of contact type, however, affected the coupon response and ultimate strength. The predicted strength of the 30° coupon with the beam offset contact (488 MPa) compared well with the test data (518 MPa and 455 MPa). The coupon with beam offset contact was linear to the predicted strength. The tiebreak coupons, on the other hand, exhibited a non-linearity in the stress-strain response seen in the experimental tests. The tiebreak contact, however, caused premature failure well below the experimental values. The perfect stack tiebreak coupon, for example, predicted a strength value 20% lower than the lowest experimental strength. Similar results were observed with the 90° coupon. Based on the results for all four simulated coupon types across the 4 testing directions, it was found that the ideally shifted coupon with the beam offset contact provided the best match to the overall composite behavior.

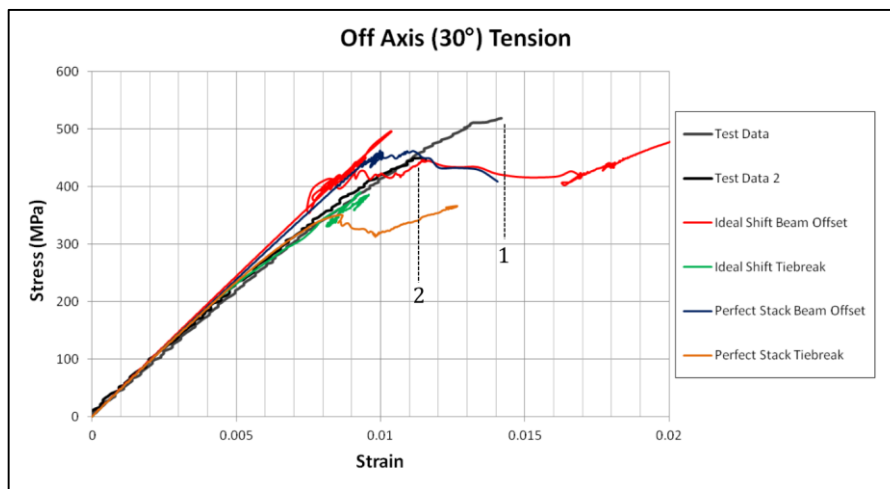


Figure 13. Stress-strain curves for the 30° coupon tensile test for both contact types and stacking configurations. The experimental data is shown in gray and black and numbered in the figure. The colored lines represent the 4 simulation coupons with varying stacking or contact type as indicated in the figure legend.

### Predicted Failure Modes

For the 0° coupon, the simulation failure occurred nearest to the grips due to the deterministic nature of the numerical solution, whereas the experiment failed both near the grips and at the gage section. The experimental curve which exhibits stiffening was a test which did not fail initially (due to insufficient grip displacement) and was subsequently reloaded. For more accurate comparison, the lower experimental test data should be used which matched well to the simulated response.

For the 30° coupon, as shown in Fig.13, the two experimental coupons exhibited a range for the predicted strength (~450 MPa and ~520MPa). The simulated coupon (ideally shifted with beam offset contact) failed initially at 495 MPa, well within the two experimental data points. The predicted failure from the simulations was



compressive failure of the bias tows oriented perpendicular to the load. A comparison between the experimental failure path and simulated failure modes is shown in Fig.14. The red elements shown are elements whose bias plies have reached their longitudinal strength. The stresses in these plies were compressive. All other plies and ply directions remained intact in the simulation coupon, hence the coupons capacity for carrying additional load (as shown by the post-peak response of the simulation in Fig.13). The experimental coupon did not show evidence of fiber tow failures aside from the compressive bias tow failures (axial tows and bias tows not perpendicular to the load were intact) and was relatively stiff compared to the other failed coupons. This stiffness and strength remaining in the simulation may be important to capturing the appropriate residual stiffness and strength of the composite post-impact and should not be dismissed. The termination of the experimental test was likely due to the significant load drop experienced during the compressive tow failure, resulting in a stop condition.

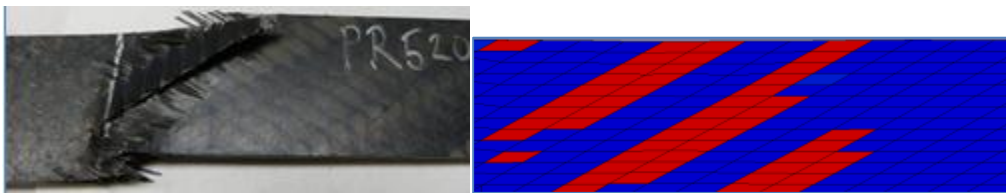


Figure 14. The experimental failure and the predicted failure of the 30° coupon. The color coding corresponds to red specifying an element whose integration point has reached the damaged state (D=1) in the longitudinal direction. The stress in these integration points (which corresponded to the bias tows lying perpendicular to the load) was compressive.

Figure 15 shows the stress-strain curves for the experimental and numerical coupons in the 60° coupon test for both the original simulation, which used the bias longitudinal strength obtained from the top down unit-cell approach, and the modified simulation which enforced a failure strain equivalent to the axial ply longitudinal direction. The modified simulation (with bias ply tensile failure strains set equal to the axial ply tensile strains) had a predicted strength of 830 MPa, correlating well with the reported experimental strengths of 828 and 862 MPa. These results are far improved from the original predictions of 464 MPa. In addition, this updated bias ply longitudinal strength did not affect the predicted strength or stress-strain response of the 0° and 30° coupon, since it was not a significant failure direction in those two directions.

The predicted failure mode of the composite for 60° coupon was tensile failure of the bias UD plies in the longitudinal direction (direction of the applied loading). This correlates well with the experiment.

The stress-strain curves for the 90° coupon are presented for both the simulation and experiments in Fig.16. Both the original simulation (which under-predicted the 60° coupon strength) and the modified simulation with updated bias ply tensile strains/strengths are presented. Although the original simulation predicted a strength value which matched well with the experimental data, the failure mode was a longitudinal failure of the bias tows. The experiment, on the other hand, was a function of edge-initiated shear failure. As a result, the increased bias tow tensile strength in the modified simulation causes an over-estimation of the composite strength in the 90° direction. The over prediction may be due to limitations of the current model which may

limit the ability of the current formulation to represent the free-edge effects in the 90° coupon.

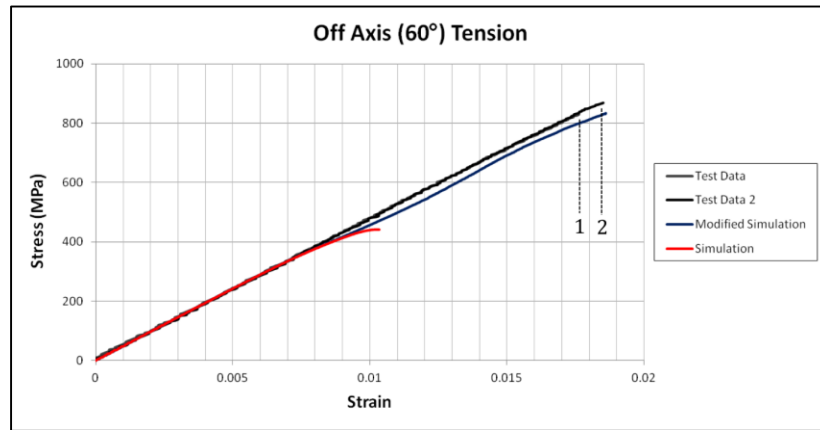


Figure 15. Stress-strain curves for the ideally shifted coupon with beam offsets in the 60° tensile test. Both the initial simulation (red) and the modified simulation (blue) which included the increased bias toward longitudinal tensile strengths are presented. Experimental data from two separate tests are shown (gray and black) with labels to distinguish the termination points.

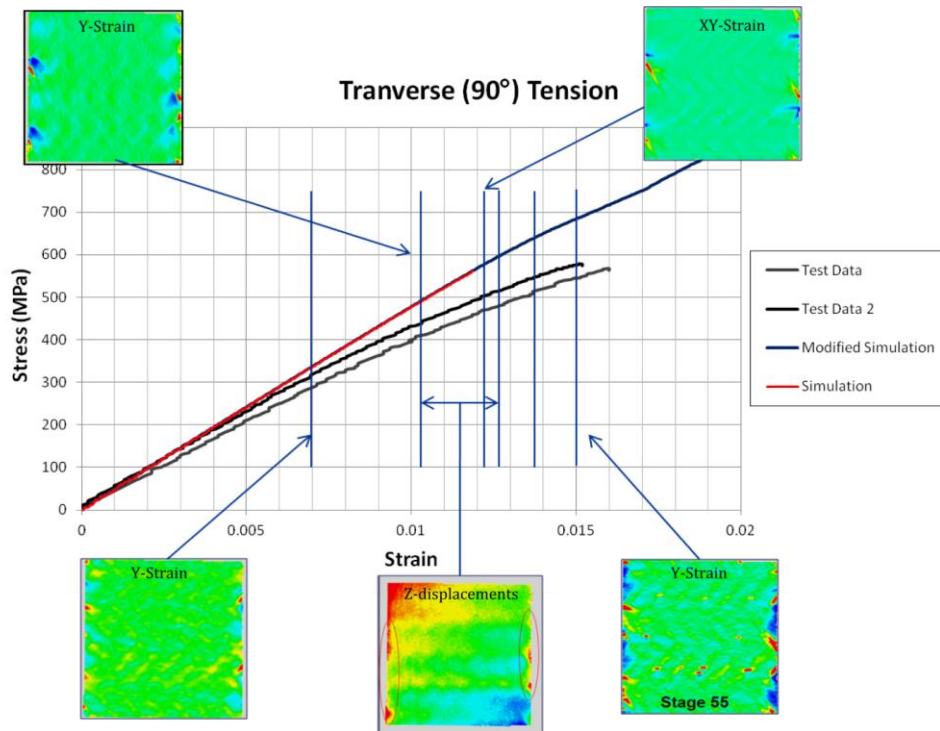


Figure 16. Stress-strain curves for the 90° coupon tensile test. Stress-strain curves for the simulation and experiment overlapped with DIC images of both the shear and longitudinal strains (w.r.t. the loading direction) at various points along the experimental curve. The vertical lines represent the onset of the observed localized strains or displacements in the experimental test. X-strain and y-strain components correspond to the axial and transverse directions, respectively.

A summary of the predicted strengths in the modified subcell model are shown in Fig.17. The results indicate that the subcell model performed well in predicting the failure mode and experimental strength for three of the four tests cases. The response of the 90° coupon which was susceptible to edge damage and hence was not captured appropriately by the FE model.

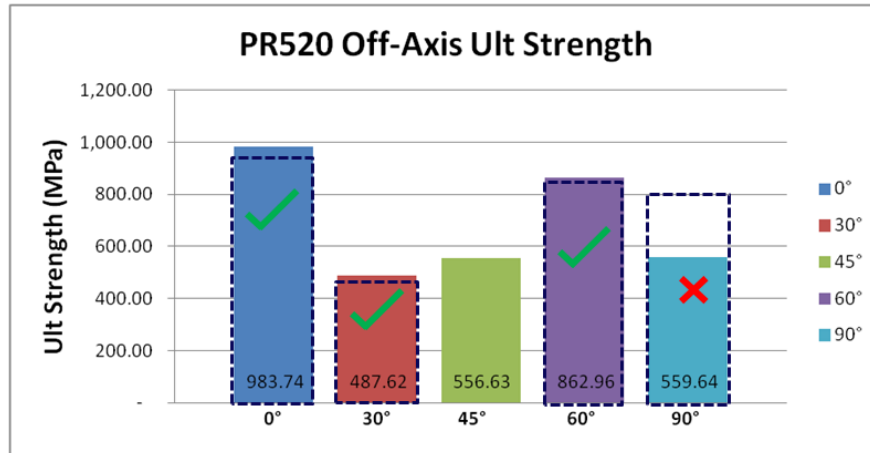


Figure 17. Comparison between the reported strength values and the modified simulation response (dashed boxes). The green check marks correspond to simulations where the failure mode in the simulation matched the observed experimental failures. The red X corresponds to a difference in failure mode predictions in the 90° coupon.

## CONCLUSIONS

A combined experimental and analytical approach has been presented to verify the proposed subcell modeling approach in capturing the behavior of 2D triaxially braided composites. The proposed modeling approach combined top down coupon level strength data with computational micromechanics to obtain model parameters.

To provide coupon level data, tensile experiments were carried using straight sided braided composite coupons loaded at five orientations. DIC was used to monitor the damage initiation and failure process during tensile tests.

A study of two different stacking configurations (through the thickness of the braid) and two different contact types assisted in identifying the most appropriate combination to accurately capture the braided coupon response. A strong contact between individual shell layers, which tied rotational and translational degrees of freedom, was found to best predict the experimental strengths. In addition, the best correlation to the experimental data was obtained for all directions when using a shifted coupon model which accounts for the nesting of axial tows observed in manufactured composites.

The subcell model was successful in predicting the failure modes and coupon strengths for the 0°, 30° and 60° coupons. A discrepancy in the original characterization of the bias tow longitudinal tensile strength was identified. The top-down methodology was modified and alternative assumptions were provided. The modified simulations provided an improved fit to the experimental data.

The result indicates that the free edge effect can significantly reduce the strength of braided composites at certain orientations. Therefore, the design and manufacturing strategies which reduce or eliminate the exposure of free edge for these orientations should lead to a significant improvement of the load bearing capability and the integrity of the structure.

In summary, the subcell approach shows promise in providing an improved analysis capability for braided composite structures with high computational efficiency. In the next phase, this approach along with the best practices reported here will be validated in the simulation of 45° coupon under tension and panel impact experiments.

## REFERENCES

1. Ayranci, C. and Carey, J. (2008) "2D braided composites: A review for stiffness critical applications." *Compos. Struct.*, 85:43–58.
2. Roberts, G. D., Goldberg, R. K., Binienda, W. K., Arnold, W. A., Littell, J. D., and Kohlman, L. W. (2009). "Characterization of triaxial braided composite material properties for impact simulation." American Helicopter Society. Grapevine, TX, USA. 2507–2528.
3. Li, X., Binienda, W. K., and Littell, J. D. (2009). "Methodology for Impact Modeling of Triaxial Braided Composites Using Shell Elements." *J. Aerosp. Eng.*, 22, 310–317.
4. Cheng, J., and Binienda, W. (2008). "Simplified Braiding through Integration Points Model for Triaxially Braided Composites." *J. Aerosp. Eng.*, 21, 152–161.
5. Goldberg, R. K., Blinzler, B. J., and Binienda, W. K. (2010). "Modification of a Macromechanical Finite Element Based Model for Impact Analysis of Triaxially Braided Composites." *J. Aerosp. Eng.*, 25, 383-394.
6. Xiao, X., Kia, H. G., and Gong, X.-J. (2011). "Strength prediction of a triaxially braided composite." *Compos Part A*, 42, 1000–1006.
7. Cater, C., Xiao, X., Goldberg, R.K., W. Kohlman, L.W. (2014). "Single and Multi-ply Braided Composite Response Predictions using Modified Subcell Approach," *J. Aerosp. Eng.*, 04014117, 1-12.
8. Blinzler, B. J. (2012). "Systematic Approach to Simulating Impact for Triaxially Braided Composites." Ph.D. thesis, University of Akron, Akron, OH.
9. Littell, J. (2008). "The Experimental and Analytical Characterization of the Macromechanical Response for Triaxial Braided Composite Materials." Ph. D. thesis, University of Akron, Akron, OH.
10. Matzenmiller, A., Lubliner, J., and Taylor, R. L. (1995). "A Constitutive Model for Anisotropic Damage in Fiber Composites." *Mech Mater*, 20, 125-152.
11. Schweizerhof, K., Weimar, K., Munz, Th., and Rottner, Th. (1998). "Crashworthiness Analysis with Enhanced Composite Material Models in LS-DYNA – Merits and Limits". 5th International LS-DYNA User's Conference, Southfield MI.
12. Bednarczyk, B. A. and Arnold, S. M. (2002). "MAC/GMC 4.0 User's Manual – Keywords Manual". NASA Technical Memorandum, NASA/TM-2002-212077/VOL2.
13. Aboudi, J., Arnold, S. M., and Bednarczyk, B. A. (2012). "Micromechanics of Composite Materials: A Generalized Multiscale Analysis Approach." Butterworth-Heinemann, Oxford, UK.
14. Kohlman, L. W. (2012). "Evaluation of Test Methods for Triaxial Braid Composites and the Development of a Large Multiaxial Test Frame for Validation Using Braided Tube Specimens." Ph.D. thesis, University of Akron, Akron, OH.
15. van der Sluis, O., Schreurs, P.J.G., Brekelmans, W.A.M. and Meijer, H.E.H. (2000). "Overall behaviour of heterogeneous elastoviscoplastic materials: effect of microstructural modeling." *Mech Mater*, 32, 449-462.
16. Goldberg, R. K, Roberts, G. D., and Gilat, A., (2003). "Implementation of an Associated Flow Rule Including Hydrostatic Stress into the High Strain Rate Deformation Analysis of Polymer Matrix Composites." NASA Technical Memorandum, NASA/TM-2003-212382.